Design and Development of a Multi-Winding High-Frequency Magnetic Link for Grid Integration of Residential Renewable Energy Systems

Mohammad Jafari*, Zahra Malekjamshidi, and Jianguo Zhu

School of Electrical and Data Engineering, Faculty of Engineering and IT, University of Technology Sydney
15 Broadway, NSW 2007, Australia
**Corresponding author, Email: Mohammad.jafari@uts.edu.au*

Abstract: **Recent advances in magnetic material characteristics and solid-state semiconductors have provided the feasibility of replacing the electrical buses with the high-frequency multi-winding magnetic links in small-scale renewable energy systems. This effectively reduces the number of conversion stages and improves the system's efficiency, cost and size. Other advantages are galvanic isolation between the ports, bidirectional power flow capability and flexibility in energy management and control. Despite the advantages, design and development of the multi-winding magnetic links is relatively complex and based on computationally expensive numerical methods. Furthermore, non-sinusoidal nature of voltage and currents, high-frequency parasitic effects and nonlinearity of magnetic material characteristics increase the design complexity. In this paper, the reluctance network modeling as a fast analytical method is used to design a three winding magnetic link. The core and copper losses of the designed component are evaluated taking into account duty ratio, amplitude and phase shift of the non-sinusoidal excitation voltage and currents. The thermal analysis is carried out using an accurate thermal-electric model. A prototype of the magnetic link was developed for application in a residential renewable energy system using amorphous magnetic materials. A set of experimental tests are conducted to measure the electrical parameters, magnetic characteristics, core loss, copper loss and temperature rise of the designed component and the results are compared to the specifications to validate the design procedure.**

Index Terms: **Copper loss, core loss, design, magnetic link, reluctance network modeling, thermal analysis, transformer**

I. Introduction

High-frequency magnetic links have attracted significant attention due to their application in grid integration of renewable energy resources. Improvements of smart micro-grid technologies have increased demands for more reliable and flexible converters and control techniques. The high frequency magnetic links can effectively combine multiple conversion stages into a single system and improve the conversion efficiency with the help of modern soft magnetic materials and low power loss solid state switching devices [1], [2]. The magnetic link is quite similar to the conventional multi-winding high frequency transformer except that it provides bidirectional paths for magnetic fluxes and power flows between different ports. The common topologies of the renewable energy systems (RESs) utilize multiple converters to link the renewable sources with different voltage levels to a common ac or dc bus [3] although, some problems such as voltage and frequency instabilities and control complexity are emerged [4]. The magnetic links are feasible replacement for traditional electrical ac and dc buses in small-scale RESs. They can be used as a common magnetic bus to integrate the sources of different voltage levels using different turn ratios [5]-[6]. They also provide galvanic isolation and the possibility of simultaneous and bidirectional power flow between the converter ports [7], [8]. Fig.1 compares two RESs with and without the magnetic link. The red dashed lines show that the power flow path from PV array to the battery has been reduced effectively with the use of the magnetic link. It can be seen that employing the magnetic link has reduced the number of voltage conversion stages, increased the system efficiency and reduced the system size and cost. Research on design, characterization and modeling of the magnetic links has attracted considerable interest in recent years due to their increasing applications [9], [10]. Despite their advantages, design of multi-winding magnetic links for certain specifications is relatively complex due to their non-linear characteristics and structural complexity [11]. Different methods of design and modeling of the magnetic components are presented in the literature [12]-[17]. The simplest methods are based on the lumped-parameter models and rely on many simplifying assumptions which reduce their accuracy [12], [13]. On the other hand, numerical methods such as finite element method (FEM) require extensive computation effort in iterative design procedures [14], [15]. Reluctance network methods (RNMs) also known as magnetic equivalent circuits (MECs) as a third option, can be used to design the components with a reasonable accuracy and computation time [16], [17]. The method is formally introduced by Laithwait [18] and Carpenter [19] in 1967 and 1968 respectively. It has been widely used in analysis and design of electrical machines [20] and 2-D and 3D analysis of the magnetic structures [21]. It also has been used to model the dynamics of the electrical machines [22],[23] and a general 3D RNM applicable to various magnetic structures is introduced in [24]. The designed structure of the magnetic component should be evaluated for core and copper losses and the temperature rise. The original Steinmetz equation (OSE) has been conventionally used to estimate the magnetic loss [25]. However, the equation is obtained for the sinusoidal excitation and needs to be modified for rectangular waveforms [26]. The modified Steinmetz equation (MSE) [27], natural Steinmetz extension (NSE) [28], improved generalized Steinmetz equation (IGSE) [29], and the waveform-coefficient Steinmetz equation (WCSE) [30], are some of the proposed modifying methods. It has been shown that the IGSE

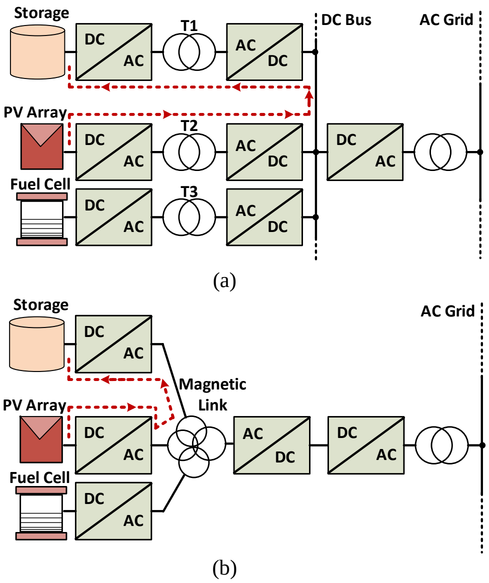

(a)

(b)

Fig. 1. Comparing two renewable energy systems, (a) without the common magnetic link and, (b) with the common magnetic link.

presents better results for estimation of the core loss in the case of the rectangular waveforms [26]. On the other hand, the copper loss analysis methods are classified as numerical [31] and analytical [32] methods. The numerical methods provide more accurate results although, they need large computation efforts. The analytical methods use the harmonic content of the excitation currents and ac resistance of the wire considering skin and proximity effects to calculate the copper loss. The amplitude of the harmonics is defined using Furrier transform while the ac resistance is defined based on the different approaches. The most common approaches are based on the Dowell's work in 1966 on loss analysis of the foil and round conductors [33]. However, some modifications are applied to the original equation in the case of the Litz wire windings [32]. The second method is known as Ferrira method and is based on the exact field analysis of a round conductor using Bessel functions [34] and is later extended to a complete winding case [35]. In the third approach the ac resistance factor is defined by complex conductor permeability [36]. On the other hand, the ac and dc resistances are highly coupled to the temperature which needs to be taken into account [37]. The designed component then is evaluated for temperature rise considering core and copper losses as the main heat sources [26]. The common thermal analysis approaches use a thermo-electric model of the magnetic component [38]. A satisfactory design procedure includes all the above mentioned stages.

This paper presents the design, development and experimental tests of a multi-winding magnetic link designed for application in a magnetically coupled residential RES. The designed component then is evaluated for equal core and copper losses to maintain the maximum efficiency taking into account limitations of temperature rise. To validate the proposed design procedure, a prototype of the magnetic link has been fabricated using amorphous magnetic materials. The main contributions of this paper can be listed as:

- Design of the magnetic link including core dimension and number of turns of each winding using the RNM by defining appropriate 3D reluctance elements and analysis domains.
- Core loss analysis considering non-sinusoidal high-frequency effects of the supplied voltages.
- Copper loss analysis of the designed structure taking into account the amplitude, duty cycle and the phase shift of the supplied currents and the high-frequency skin and proximity effects.
- Thermal analysis of the magnetic link using a thermo-electric model of the designed component.
- Introducing an experimental method for measuring the magnetic link parameters by using differentially and cumulatively series coupling tests.

The rest of the paper is organized as follows. The application of the magnetic link in the proposed RES and its equivalent electrical model are presented in sections II and III respectively. Details of the magnetic link design are discussed in section IV, and experimental test results are presented in section V. A conclusion is derived in section VI.

II. Application of the Magnetic Link

The proposed magnetic link is employed in a residential RES to integrate the energies of a PV, a fuel cell stack and a battery to supply the loads as presented in Fig.2. It can operate in multiple operation modes in grid-connected and off-grid conditions. The system includes a triple-active bridge phase shift dc-dc converter, a buck-boost bidirectional converter, an interleaved boost converter and a grid-connected single-phase inverter. The proposed system is developed experimentally as presented in Fig.3. It is designed to supply a 4.5 kW residential load by combining the energies of a PV array, a fuel cell stack and a battery bank. The system is controlled by two Texas instrument DSPs (C2000/TMS320F28335) as local controllers and a PC as master controller and energy management unit (EMU). The EMU communicates with the regional power distribution control center to manage the energy of the system based on the short-term and long-term plans. The phase shift converter includes three H-bridge conversion cells to generate a high frequency square-wave voltage from a dc bus and apply it to the corresponding winding of the magnetic link. The voltages of ports two and three are shifted for a leading or lagging phase angle respected to port one to send or receive power to/from the inverter and further to the residential load and grid. Port one is a bi-directional port and is used in the reverse direction to transfer the power from the grid to the battery (using ports two and four simultaneously). An interleaved boost converter is used to link the PV to the magnetic link. To extract the maximum possible power from the PV array, a duty cycle control is applied to the switching devices in port three (S31-S34). The fuel cell is directly connected to a 50-70 V dc bus links in port two and the 24 V battery bank is linked via a bi-directional buck-boost converter. It can be charged by fuel cell, PV or grid. The magnetic link provides isolation and flexible

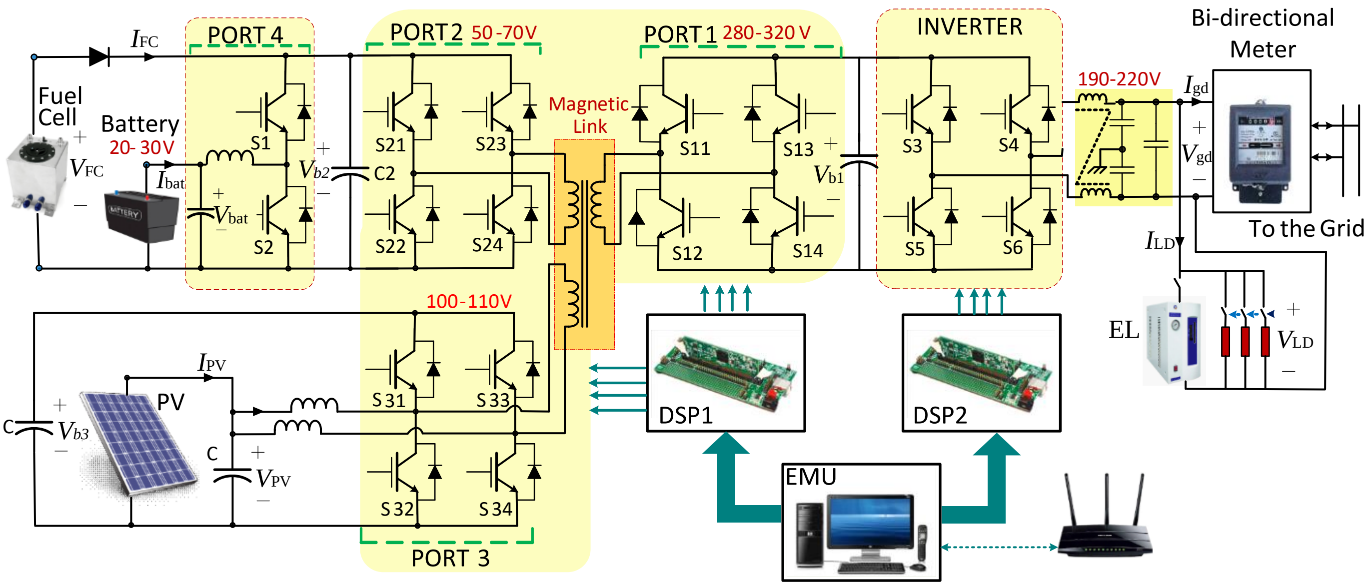

Fig. 2. Structure of the proposed residential renewable energy system.

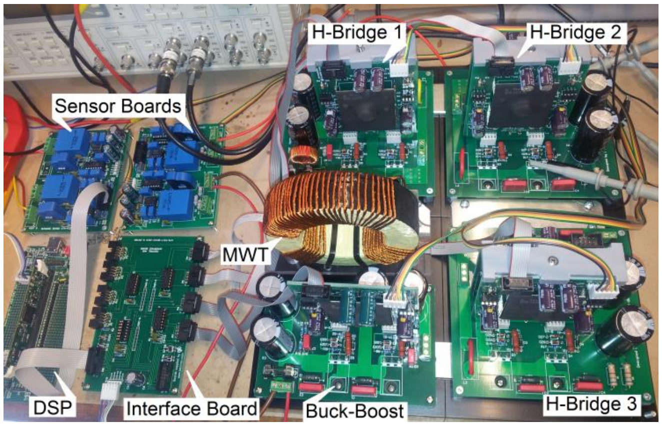

Fig. 3. Experimental set of the designed renewable energy system.

power flow direction between the ports. It facilitates operation of the system in different modes and various energy management scenarios in both grid-connected and islanded conditions. The rectangular voltages generated by H-ridge converters fed to the windings may have a variable duty cycle, amplitude and phase shifts which should be taken into account in the design procedure. The voltage in port one is used as a reference and has a constant amplitude (320V) and duty cycle (D1=1). On the other hand, voltage of port three (PV port) has a variable phase shift, amplitude and duty cycle due to the MPPT requirement. The voltage of winding two is almost constant in amplitude and duty cycle (D2=1) as the battery is used as dc voltage stabilizer due to the slow dynamic response of the fuel cell.

III. Equivalent Electrical Model of the Magnetic Link

In this section, an equivalent electrical circuit model is defined for the multi-winding magnetic link. As the model is derived based on winding flux linkages, it can be applied to other types of multi-winding magnetic structures. However, a toroidal core is used in this paper.

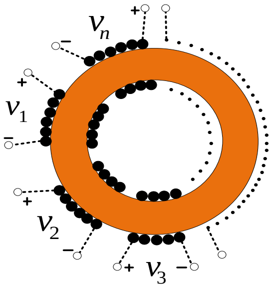

Fig. 4. Toroidal magnetic link including *n* windings.

Assume *n* separate windings distributed unsymmetrical around a toroidal core as presented in Fig.4. The voltage of each winding can be calculated using Faraday's law based on its current *i*, resistance R_W, and flux linkage λ_{ij} from

$$v_i = i_i R_{W_i} + \sum_{j=1}^{n} \frac{d\lambda_{ij}}{dt}, \quad for\ i = 1,2,...,n \tag{1}$$

Considering winding one as the reference, all parameters of other windings, including self (i=j) and mutual (i≠j) inductances, winding's resistances, voltages and currents can be referred to the winding one. The series connection of magnetizing inductance (L_m) and the core loss equivalent resistance (R_m) is referred although, their parallel connection, (L'_m, R'_m) is preferred from the physical perspective. The series connection facilitates the analysis of series-coupling tests on the windings [39] as will be discussed in section V. The parallel-to-series transform equations can be written as

$$R_m = \frac{R'_m \omega^2 (L'_m)^2}{(R'_m)^2 + \omega^2 (L'_m)^2} \tag{2}$$

$$L_m = \frac{(R'_m)^2 L'_m}{(R'_m)^2 + \omega^2 (L'_m)^2} \tag{3}$$

Applying (1) to the all *n* windings of the magnetic link, the final equation of voltages applied to the windings can be rewritten as

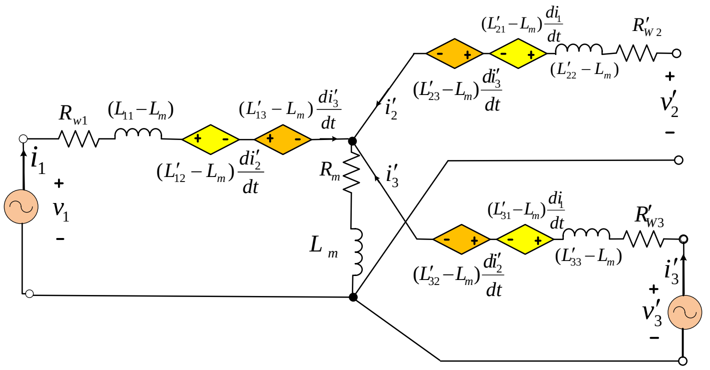

Fig. 5. The equivalent electrical model of a three winding magnetic link

$$V=\tilde{R}I+\tilde{L}\frac{dI}{dt} \tag{4}$$

where V, I, $\tilde{L}$ and $\tilde{R}$ are the voltage, current, inductance and resistance matrices of the windings and are defined as

$$V=\begin{bmatrix} v_1 \\ v'_2 \\ . \\ . \\ v'_n \end{bmatrix},\quad \tilde{L}=\begin{bmatrix} L_{11}-L_m & L'_{12}-L_m & . & L'_{1n}-L_m & L_m \\ L'_{21}-L_m & . & . & . & L_m \\ . & . & . & . & . \\ . & . & . & . & L_m \\ L'_{n1}-L_m & L'_{n2}-L_m & . & L'_{nn}-L_m & L_m \end{bmatrix}$$

$$I=\begin{bmatrix} i_1 \\ i'_2 \\ . \\ . \\ i'_n \\ i_m \end{bmatrix},\quad \tilde{R}=\begin{bmatrix} R_{W1} & 0 & 0 & . & 0 & R_m \\ 0 & R'_{W2} & 0 & . & 0 & R_m \\ . & . & . & . & . & . \\ . & . & . & R_{W(n-1)} & 0 & R_m \\ 0 & 0 & . & 0 & R_{Wn} & R_m \end{bmatrix} \tag{5}$$

A model of the three winding magnetic link based on (4) is presented in Fig. 5. The resultant model will be used later in the experimental tests.

IV. Design Stages of the Magnetic Link

Design of multi-winding magnetic components for certain values of parameters using classical methods of transformer design relies on many simplifying assumptions, which affect the accuracy of the results. More accurate numerical methods such as finite element method (FEM) and RNM have been widely used in the design of transformers and electrical motors. The FEM is an accurate field analysis method, although it is computationally expensive and is not preferred for design optimization iterative procedures [21]. On the other hand, the RNM requires less computation time but loses its accuracy, especially in the case of magnetic components with complex structure [16], [17]. The FEM can introduce the nonlinearity of magnetic materials, geometry and actual winding distribution into the design process while RNM is based on linear assumptions. Therefore, design and optimization of magnetic components using RNM are reliable for the operation of the system in the linear area of B-H curve. The RNM is used in this research to design the magnetic link due to the iterative nature of the design procedure. To increase the accuracy of numerical calculations various computation domains and constraints are selected.

The design stages of the magnetic link are illustrated in Fig.6. As can be seen, the design process begins with the introduction of user-defined parameters such as winding's turns ratio, magnetic material characteristics, rated power, voltage, current and frequency. To select the magnetic materials, different possible options are studied. The soft ferrites have low saturation flux density (0.3-0.5 T) which results in the large transformer size although they have been widely used in high-frequency converters due to their low price and availability. Nano-crystalline materials and amorphous alloys as other possible options have presented lower core loss, higher saturation flux density and higher permeability. Comparing their characteristics shows that nano-crystalline materials have lower saturation flux density (0.8-1 T) than the amorphous alloys (1.4-1.6 T) and presents lower core loss [40]. The amorphous alloy Metglas-2605SA1 made by Hitachi metals is finally selected considering maximum flux density, specific core loss, cost and availability. As the value of leakage inductances are essential for proper operation of the system, the required values of leakage and self-inductance of the windings are selected as the design specifications. On the other hand, the number of turns, dimension of the magnetic core, and thickness of the insulator between each winding and the core are selected as the design variables. The electrical parameters of the magnetic link which are used as design specifications are presented in TABLE. III/Appendix.

At the first stage, the initial values of the design variables are defined using classical methods of transformer design [41]. The power handling capacity, current density and flux density are used to find the area-product of the core, and then the core size was selected using the area-product/core-size chart. The resultant values from the first stage of the design are used to define a proper variation range for the design variables in the second stage and reduce the total time of the design process.

A. Design of magnetic link geometry using RNM

In the second stage, the field analysis of the magnetic structure using RNM was carried out to calculate the magnetic flow φ, flux density B, field intensity H, and finally define the geometry and dimension of the magnetic link. The resulting values of B and H are used to calculate the winding self-inductances L_{11}, L_{22}, L_{33} and leakage inductances L_{l1}, L_{l2} and L_{l3} as the main design objective. The magnetic link should be designed for certain values of leakage inductances as they are used as energy transfer components in the proposed system. Using external bulked inductors in series with the transformer windings is suggested although it increases the size and cost of the converter [8].

As can be seen in Fig.6, the steps of RNM based field analysis are enclosed by dashed lines. The core geometry and number of turns of each winding were selected based on initial design. The design process is based on the operation in the linear section of the magnetization curve and the amplitude of terminal voltage was chosen such that the peak flux density would just reach the knee point of the magnetizing curve. Therefore, the excessive magnetization current, extra current harmonics and core losses due to the distortion of the magnetic field are avoided. To start the field analysis, the magnetic structure is partitioned into three different areas, including a magnetic core, covering insulator and the free space around the core. The windings effect is not included in the analysis due to the complexity of flux distribution inside the conductors and difficulty of their modeling using RNM. Considering the operation of the magnetic structure in the linear section of the magnetization curve, a constant value of permeability is used for analysis. The cylindrical coordinate system was selected for numerical modeling due to the axial symmetry of the toroidal core. The core is partitioned into

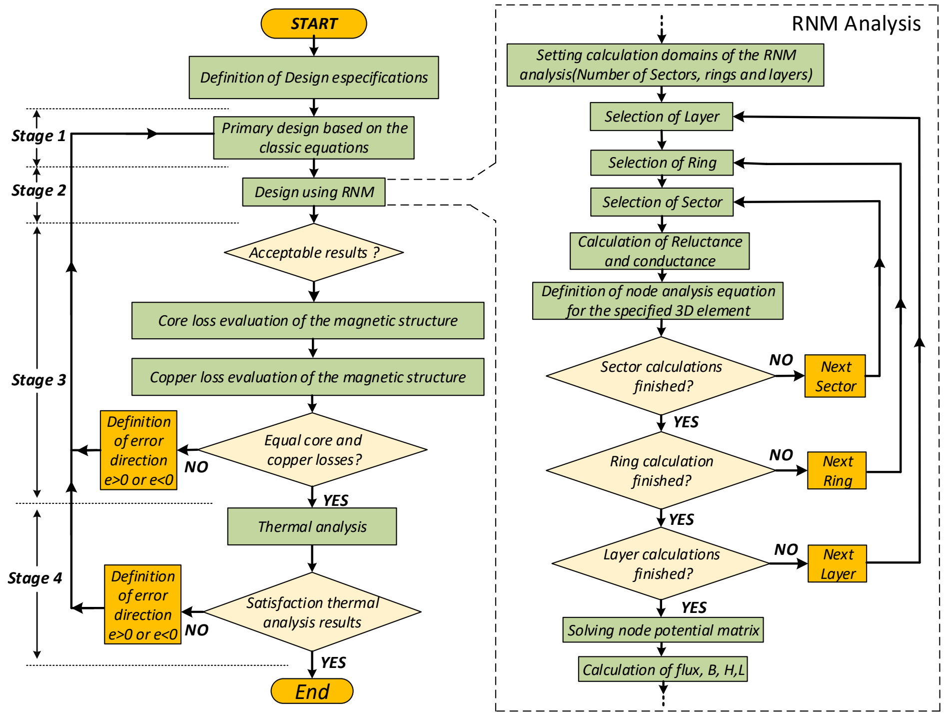

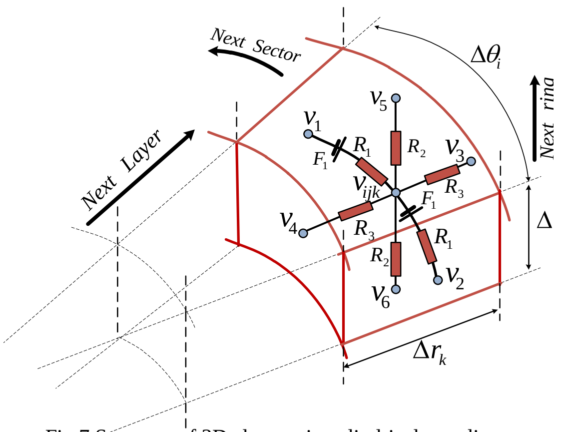

Fig.7 Structure of 3D element in cylindrical coordinate

Fig.6.The design stages of the magnetic link using MATLAB

thousands of 3D elements arranged in sectors in θ, layers in radial r, and rings in Z directions as presented in Fig.7. Each element presented by Q_{ijk} , where indexes, i, j and k represent the unique situation of the 3D element among the entire magnetic structure. The element includes six reluctances linked to a central node at one side and to the boundary nodes at the boundary surfaces of the element at the other side. The calculation domains such as number of sectors, rings and layers are defined at first step. The RNM analysis starts with the first sector of the first ring of the first layer and the next ring is selected when all sectors are analyzed, and the next layer is selected when analysis of all rings of the previous layer is completed. The reluctances are defined based on the permeability factor of the element and its geometrical shape. The sources F_{ijk} , are representative of magneto-motive force *mmf*, in the corresponding direction. Their value in directions of r and Z is almost zero and in θ direction depends on the number of turns of the winding covering the element and the current flowing through it. The current flowing through each resistor represents the magnetic flow in that direction and can be calculated by applying nodal analysis to the element. The potential of the central nodes of the elements situated on the boundary layers and rings are assumed to be zero as an initial condition. The resultant equations with the voltage of the central nodes as unknown were solved using MATLAB. In a branch b (b=1, 2, 3,…, 6 based on Fig.7), the field intensity, H_b the flux density B_b, and the volume V_b can be defined from

$$H_b=(v_{ijk}-v_b-F_b)/l_b,\quad B_b=\varphi_b/A_b,\ V_b=A_b l_b \tag{6}$$

where A_b and l_b are branch cross-section and length respectively [22]. The total energy of a 3D element is defined by closed-form volumetric integral from

$$W_S=\int_V \frac{H.B}{2}dV=\frac{\mu}{2}\int_V |H|^2 dV \tag{7}$$

where W_S is the stored energy in the enclosed volume V, and μ is the magnetic permeability. Assuming almost constant flux density in the element, the net magnetic energy stored in the b-th branch using (7) is defined from

$$W_b=\mu V_b H_b^2/2 \tag{8}$$

Substituting (6) into (8) results in

$$W_i=(v_{ijk}-v_b-F_b)^2/2R_b \tag{9}$$

where R_b and F_b are the reluctance and *mmf* of the branch respectively. The value F_b, should be equal to zero for branches without *mmf*. The equivalent inductances of windings can be defined using the well-known energy method [22], [24]. To calculate the winding self-inductances, a surface enclosing the entire magnetic structure is assumed. The total enclosed energy is calculated by integrating the energy of all elements inside the surface and the energy of each element can be calculated by integration of the energy in all six branches of the element. The resultant total energy W_S, and the winding current I_s, are used to define the equivalent inductance L_{eq}, from

$$L_{eq}=\frac{2W_S}{I_s^2} \tag{10}$$

To define the leakage inductance, two different surfaces, one enclosing the winding and the core only and the second one covering winding, core and the surrounding area are considered. The leakage inductance is defined using the difference between the stored energies of the two surfaces. The value of self and the leakage inductances of all windings (L_{11}, L_{22}, L_{33}, L_{l1}, L_{l2} and L_{l3}) are calculated by using the method outlined above. Proper selection of the number of sectors, layers and rings will result in acceptable computation time and accuracy. In this research the entire magnetic link was partitioned into 22176 elements (72 sectors in θ direction, 14 rings in Z direction and 22 layers in radial direction are selected) and the total computation time was about 310 seconds using an office computer (*CPU: 64 bit/3.1 GHz Intel Core i5-2400, RAM: 4.00GB*). The resultant magnetic structure then is evaluated for core and copper losses in the third stage of the design as illustrated in Fig.6.

B. Core loss analysis

The core and copper losses are highly dependent on the waveforms of the voltage and current of the windings. To calculate the core loss, empirical loss-expressions are used due to the simplicity and non-linear relation of the magnetic loss density and the magnetic induction. The original Steinmetz equation (OSE) has been conventionally used to estimate the magnetic loss and is presented as

$$P_v = kf^{\,m} B_{\max}^{n} \tag{11}$$

where P_v is the magnetic loss density in watts per cubic meter, f is the frequency in kilohertz and B_{max} is the maximum magnitude of flux density in Tesla. The constant coefficients k, m and n are determined by material characteristics and are normally provided by manufacturers for sinusoidal waveforms. Therefore, several time-dependent expressions have been proposed to modify the Steinmetz equation for non-sinusoidal excitation waveforms [28], [30]. Fig.8 shows the waveform of the rectangular voltage generated in the PV port and the resultant magnetic induction. To find the modified equations, the rectangular waveforms of the voltage generated by H-Bridge converters and the resultant magnetic induction are modeled using piecewise linear equations and applied to the OSE [26]. As an example, the modified equations of IGSE and WCSE are presented as (12) and (13) respectively [26].

$$P_v = 2^{n+m} k_i f^{\,m} B_{\max}^{n} D^{n-m+1} \tag{12}$$

$$P_v = (\pi/4)(1+\Omega/\pi) k f^{\,m} B_{\max}^{n} D^{n} \tag{13}$$

where B_{max} is the maximum flux density in the case of rectangular excitation voltage, k_i is the modified value of k, Ω is the zero voltage angle of the rectangular waveform as presented in Fig.8, and D is the duty ratio and is defined from

$$D = (1-\Omega/\pi) \tag{14}$$

where value of zero voltage angle, Ω is defined based on the variation range of the voltage connected to the port from

$$\Omega = \pi(V_P - V_{P-\min})/V_P \tag{15}$$

where V_P is the actual and $V_{P\text{-}min}$ the minimum voltage of the port. In the case of the PV port, considering $V_{p\text{-}min}$=30 V, and $V_{p\text{-}max}$=120 V then Ω_{min}= 0 and Ω_{max}= 3π/4 using (15). The core loss evaluation modified methods have been simulated and experimentally tested for phase shift converter application and the MSE and IGSE have been selected as the most suitable based on the experimental measurements [26]. The IGSE is used in this research to calculate the core loss in the magnetic link excited by a variable duty ratio voltage source. The values of constant coefficients m, n and k_i are suggested in [26] based on the experimental measurements for the frequency of 1 kHz for Metglas amorphous alloy 2605SA1. They are initially used in our design although to check the validity of the coefficients, an experimental test was conducted on the experimentally developed magnetic link. The core loss was measured for three cases of 10, 30 and 50 kHz as the fundamental, second and third harmonics of the applied voltages. Applying curve fitting to the results showed slight changes in the coefficients as presented in Table I. The core loss calculations are carried out for the nominal load presented in Table. III/Appendix. Details of the experimental core loss measurement are discussed in section V.

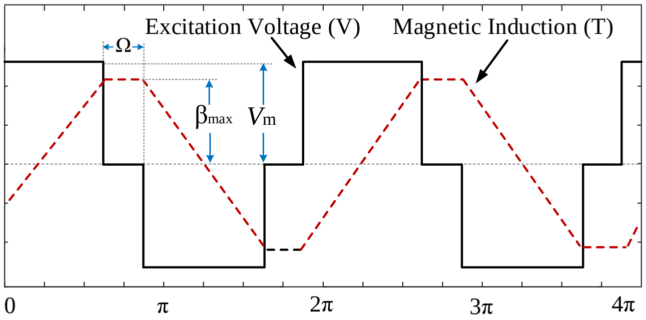

Fig.8. The waveforms of voltage and magnetic induction for Ω=$\pi/3$.

Table. I. Coefficients of Steinmetz equation

Coefficient	***k***	***m***	***n***
Original Steinmetz equation (Sinusoidal)	K=6.500	1.51	1.74
Suggested in reference [26] (square f= 1 kHz)	K_i=0.62	1.51	1.74
Experimentally measured (Square f= 10 kHz)	K_i=0.58	1.58	1.62

C. Copper loss analysis

The copper loss in the high-frequency range is increased due to the skin and proximity effects. To reduce these effects the stranded, twisted and isolated conductors known as Litz wires are recommended. The resultant losses from the skin and proximity effects in a conductor can be calculated separately due to their orthogonality considering harmonic contents of the winding current. The harmonic analysis shows that the rectangular voltages and the resultant currents in the magnetic link contain only the odd harmonics. To define the harmonics with the higher impact on the copper loss, the harmonic spectrum of the current in winding one (inverter port) for the maximum *rms* current condition (φ_{21} = φ31= π/2 and Ω=3π/4) is presented in Fig.9. To calculate the skin and proximity effects, only the harmonics with considerable effect are considered (harmonics: 1, 3, 5, …, 11) [30]. To calculate the copper loss, the ac resistance of each winding (R_{ac}) should be calculated. The ac resistance of a winding is a function of frequency due to the high-frequency skin and proximity effects however, the dc resistance R_{dc} is relatively constant and can be defined from

$$R_{dc} = \frac{4Nl_s\rho_{Cu}}{n_s\pi d_{str}^2} \tag{16}$$

where N is the number of turns of a winding, l_s the average length of one turn, ρ_{cu} the resistivity of copper, n_s the number of strands and d_{str} the strand diameter. The ratio of $R_{ac,n}$ to R_{dc} known as ac resistance factor, $F_{r,n}$, can be defined as

$$F_{r,n} = \frac{R_{ac,n}}{R_{dc}} \tag{17}$$

The copper loss of each winding, for n-th harmonic assuming Litz wire conductors, can be calculated from

$$P_{cu,n} = \left(\frac{I_n}{\sqrt{2}}\right)^2 F_{r,n} R_{dc} \tag{18}$$

where R_{dc} is the dc resistance of the Litz wire winding, I_n is the peak value of the harmonic amplitude of the current under nominal load condition and $F_{r,n}$ is the ac resistance factor of the harmonic. The total copper loss in each winding then can be found by integrating the losses attributed to the all the harmonics or the main harmonics from

$$P_{cu} = \sum_{i=1}^{n} P_{cu,n} \tag{19}$$

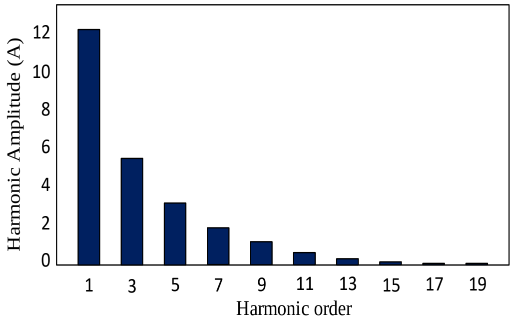

Fig. 9. The harmonic content of the current in port one for f=10 kHz, V1=360 V, V2=55 V, V3=100 V, $\varphi_{21}=\varphi_{31}=\pi/2$ and $\Omega=0$.

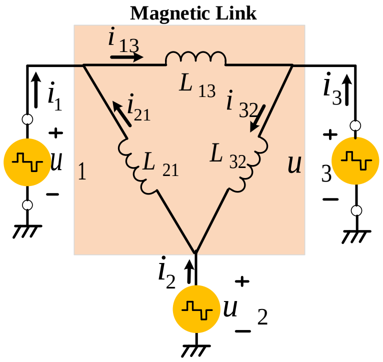

Fig.10. The Δ-model equivalent circuit of the three winding magnetic link.

To find the harmonic content of the current in the windings, the simplified equivalent Δ-model circuit of the magnetic link should be used. In this model the H-bridge conversion cells and the generated square wave voltages are modeled as ac voltage sources as presented in Fig.10. The T-model of the three winding magnetic link presented in Fig.5, can be transformed to the equivalent Δ-model assuming ($L_m=L_{ij}$, $R'_m=\infty$ and $R_w=0$). The resultant model shows that a triple active bridge (TAB) phase shift converter can be modeled and analyzed as three dual active bridge (DAB) converters. The leading phase shift angles φ_{21} and φ_{31} are assumed between ports two and three to port one respectively and their variation range is limited between 0 to π/2. The zero voltage angle, Ω is varied to control the duty ratio of voltage, u_3 in the PV port (Port three). To calculate the copper loss, the *RMS* values of the currents in the windings which are equal to the source currents i_1, i_2 and i_3 should be calculated. They can be found using currents in the equivalent inductances of the Δ-model presented as i_{12}, i_{31} and i_{21}. As an example, the waveforms of the voltages and currents required to calculate i_1. are presented in Fig.11. Due to the complexity of analysis based on the geometrical shape of the waveforms, harmonic base analysis using phasors is preferred [26]. Fig.12 illustrates the fundamental harmonic phasor diagram of the voltages and currents in the equivalent Δ-model.

To carry out the analysis, the high-frequency square wave voltages in the equivalent Δ-model are represented based on their Fourier series as

$$\begin{aligned} v_1(t) &= \sum_{n=1}^{\infty} V_{1,n}\sin(n\omega t) \\ v_2(t) &= \sum_{n=1}^{\infty} V_{2,n}\sin(n(\omega t+\alpha)) \\ v_3(t) &= \sum_{n=1}^{\infty} V_{3,n}\sin(n(\omega t+\beta)) \end{aligned} \tag{20}$$

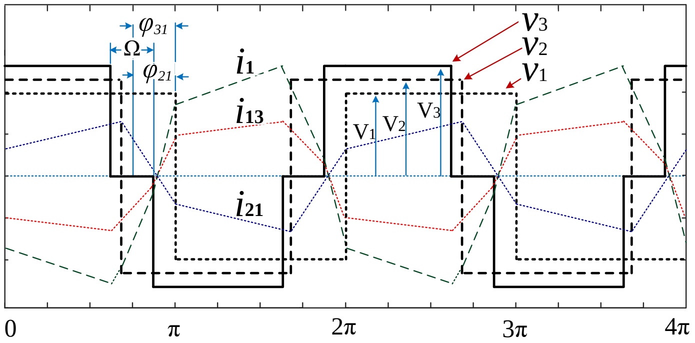

Fig.11. Voltage and current wave forms related to current i_1 in winding one.

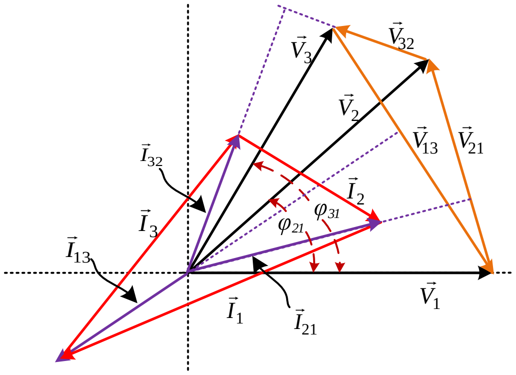

Fig. 12. Fundamental phasor diagram of the three port converter

where $V_{i,n}$ is the amplitude of the n-th harmonic of the voltage across winding and can be defined from (21) for port one and two due to their constant amplitude and duty ratio and from (22) for port three due to its variable amplitude and duty ratio.

$$V_{k,n}=\frac{2V_k(1-\cos(n\pi))}{n\pi},\qquad k=1,2 \tag{21}$$

$$V_{3,n}=\frac{2V_{3-\min}\cos(n\Omega/2)(1-\cos(n\pi))}{n(\pi-\Omega)} \tag{22}$$

According to the presented Δ-model, to find the current i_1, the currents i_{21} and i_{13} should be calculated using voltage difference across inductances L_{21} and L_{13}. The voltage v_{21} can be calculated using (17) from

$$v_{21}(t)=v_2(t)-v_1(t)=\sum_{n=1}^{\infty}V_{21,n}\cos(n\omega t+\alpha_n) \tag{23}$$

with the amplitude of n-th harmonic ($V_{21,n}$) is defined from

$$V_{21,n}=\sqrt{V_{1,n}^2+V_{2,n}^2-2V_{1,n}V_{2,n}\cos(n\varphi_{21})} \tag{24}$$

and the phase angle of n-th harmonic as

$$\alpha_n=\tan^{-1}\frac{V_{2,n}\sin(n\varphi_{21})}{V_{2,n}\cos(n\varphi_{21})-V_{1,n}} \tag{25}$$

The current i_{21} assuming π/2 as inductive phase angle can be calculated from

$$i_{21,n}=\sum_{n=1}^{\infty}I_{21,n}\sin(n\omega t+\alpha_n-\frac{\pi}{2}) \tag{26}$$

where $I_{21,n}$ is the amplitude of the n-th harmonic of i_{21} and is defined from

$$I_{21,n}=\frac{V_{21,n}}{(2\pi nfL_{21})} \tag{27}$$

The current in the winding L_{13} presented as i_{13} is defined similarly considering φ_{31} as the phase shift angle between v_3 and v_1, $I_{13,n}$ as amplitude and (β_n-π/2) as phase angle of n-th harmonic.

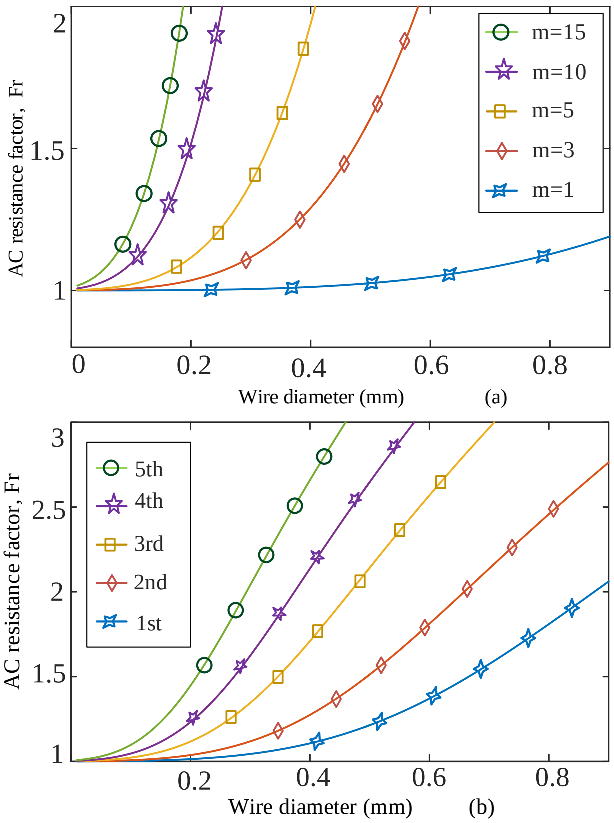

Fig.13. AC resistance factor as a function of wire diameter for: (a) different number of winding layers, and (b) various harmonics of the current in windings of the magnetic link (f=10 kHz)

$$i_{13,n}=\sum_{n=1}^{\infty} I_{13,n}\sin(n\omega t+\beta_n-\frac{\pi}{2}) \tag{28}$$

The current $i_{1,n}$ supplied by v_1 (referring to Fig.10) can be calculated using (26) and (28) from

$$i_{1,n}(t)=i_{13,n}-i_{21,n}=I_{1,n}\sin(n\omega t+\psi_{1,n}) \tag{29}$$

where $I_{1,n}$ is the amplitude of n-th har n,ic and $\psi_{1,n}$, the phase angle are defined from

$$I_{1,n}=\sqrt{I_{13,n}^2+I_{21,n}^2-2I_{13,n}I_{21,n}\cos(n(\beta_n-\alpha_n))} \tag{30}$$

$$\psi_{1,n}=\tan^{-1}\left(\frac{I_{13,n}\sin(n\beta_n)-I_{21,n}\sin(n\alpha_n)}{I_{13,n}\cos(n\beta_n)-I_{21,n}\cos(n\alpha_n)}\right) \tag{31}$$

The harmonics of the current in winding two ($i_{2,n}$) and three ($i_{3,n}$) can be found similarly. Once the amplitude of the harmonics of the current in the windings ($i_{1,n}$, $i_{2,n}$ and $i_{3,n}$) are determined, the ac resistance of each winding, $R_{ac,n}$, attributed to each harmonic should be defined for loss analysis.

In this paper, the ac resistance factor is defined based on Dowell's equation for ac resistance of round conductors [33]. The equation for ac resistance factor ($F_{r,n}$) of the m-th layer of round conductors is defined as

$$F_{r,n}=\zeta_n\left[\upsilon_{1,n}+\frac{2(m^2-1)}{3}\upsilon_{2,n}\right] \tag{32}$$

where

$$\upsilon_{1,n}=\frac{\sinh(2\zeta_n)+\sin(2\zeta_n)}{\cosh(2\zeta_n)-\cos(2\zeta_n)}\ ,\ \upsilon_{2,n}=\frac{\sinh(\zeta_n)-\sin(\zeta_n)}{\cosh(\zeta_n)+\cos(\zeta_n)} \tag{33}$$

$$\zeta_n=(\frac{\pi}{4})^{0.75}\frac{d}{\delta_n}\sqrt{\eta}\ ,\ \eta=\frac{d}{p} \tag{34}$$

and d is the conductor diameter, η the porosity factor of round conductor, and p the distance between centers of two adjacent conductors. The skin depth of round conductor of the n-th harmonic, δ_n, is defined by

$$\delta_n=\sqrt{\frac{\rho_{Cu}}{\pi\mu_0 nf}} \tag{35}$$

where μ_o is the permeability of free space and f the frequency of the waveform. The equation (19) can be simplified using Tailor-series for $\zeta_n\leq 2$ as

$$F_{r,n}\approx 1+\frac{(5m^2-1)}{45}\xi_n^4 \tag{36}$$

To adapt the round conductor equation (32) to the Litz wire application, the number of layers m and the penetration ratio ζ_n are replaced with the effective number of Litz wire layers m_l and $\zeta_{str,n}$ from

$$m_l=m\sqrt{n_s} \tag{37}$$

and

$$\zeta_{str,n}=(\frac{\pi}{4})^{0.75}\frac{d_{str}}{\delta_n}\sqrt{\eta_{str}} \tag{38}$$

where η_{str} is the porosity factor of Litz wire [32]. It can be seen that the frequency of the harmonic, number of winding layers and the strand diameter are the main parameters affecting the ac resistance factor. Fig.13 shows the dependency of $F_{r,n}$ to the number of winding layers and harmonic frequency (f=10 kHz). As can be seen, $F_{r,n}$ increases considerably with increasing the number of layers and the harmonic order.

The copper loss of the magnetic link for two cases of DAB and TAB operation modes is calculated based on the discussed method. In the case of the DAB mode, only the PV port supplies the inverter port and fuel cell port is deactivated. Fig.14 (a) illustrates the resultant copper loss where at the PV port (port three) the zero-voltage angle (Ω) changes from 0 to 3π/4 (assuming the PV bus voltage changes from 30V to 120V) and φ_{31} from 0 to π/2. As can be seen, in general, any increase in the phase shift angle and zero-voltage angle increases the loss however; the effect of the phase shift angle is more considerable compared to the zero-voltage angle. The zero-voltage angle has more effects on copper loss at higher phase shift angles as increasing the zero-voltage angle at higher phase shift angles raises the harmonic amplitudes considerably. The copper loss is maximized at Ω=3π/4 and φ_{31}=π/2. In the TAB operation mode, both fuel cell and PV ports are active and send their power to the inverter port. The fuel cell port is operating with the constant phase shift angle and duty ratio (φ_{21}=π/2, D=1) due to the constant voltage of the bus while the zero-voltage and phase shift angles at the PV port vary similarly to the previous case. The overall copper loss of the magnetic link is presented in Fig.14 (b). It can be seen that increasing zero-voltage angle **Ω**, increases the copper loss for entire range of the phase shift angle. The copper loss is minimized at $\varphi_{31}=\varphi_{21}/2$. The reason is that with increasing the phase shift φ_{31}, the power flow from PV to the inverter port increases and the power flow from the fuel cell to the PV port decreases as $\varphi_{23}=\varphi_{21}-\varphi_{31}$ and φ_{21} remains constant. When $\varphi_{31}=\varphi_{21}/2$ at the PV port, the power received from the fuel cell and sent to the inverter are equal, and the PV port power flow and consequently copper loss is minimized. This is presented in Fig.15 for more clarification.

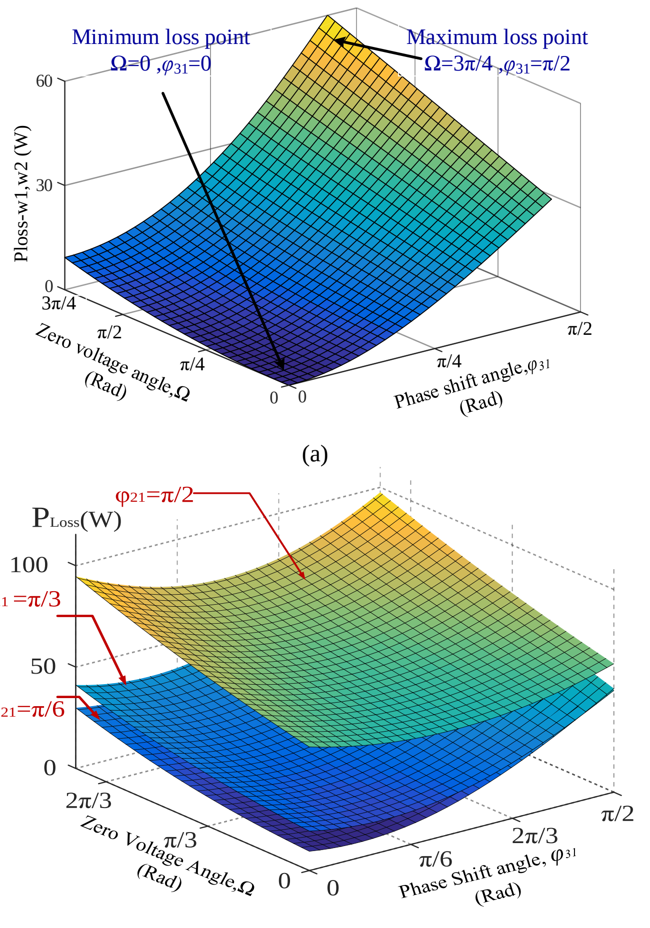

(a)

(b)

Fig.14. Calculated copper loss based on the phase shift angle and zero-voltage angle, (a)-DAB mode and, (b)-TAB mode

The core and copper losses of the magnetic link under the nominal load condition were evaluated based on the outlined methods. According to the design flowchart presented in Fig.6, the resultant values of core and copper loss should be almost equal for nominal load condition taking into account effects of Ω, φ_{21} and φ_{31} to achieve the maximum efficiency of the magnetic link. In the case of a difference of more than 10 % of total loss the magnetic core dimensions should be changed accordingly. Increasing the core dimension results in the less core loss and higher copper loss and vice versa. The resultant structure then is analyzed for thermal rise range.

D. Thermal analysis

The last stage of the design is the thermal evaluation of the designed structure which aims to ensure that the temperature rise resulting from losses remains within the acceptable range. The core and copper losses increase the temperature of the magnetic link during operation. The maximum temperature rise (ΔT) considered for the magnetic link is 45ºC in ambient temperature (T_{amb}) of 30ºC as reference. The heat transfer mechanisms of conduction, convection and radiation are considered to find the temperature rise. The thermal-electric analogy has been widely used for heat transfer analysis of the magnetic structures [38]. In this method, the winding and the magnetic core are modeled as heat sources of the system are modeled as current sources and insulation layers are modeled as thermal resistors due to their poor thermal conductivity. Fig.16 illustrates the thermo-electric model of the magnetic link applied to the axial slice geometry of the component. As can be seen in the figure, a separate equivalent thermal resistor is considered for each of the four surfaces of the core due to the uneven distribution of the temperature field. The heat flow in the top and bottom surfaces of the core are analyzed in cylindrical coordinate [38]. The thermal analysis parameters are illustrated in Table.III/Appendix. The thermal resistance of the top and bottom insulation layers can be calculated from

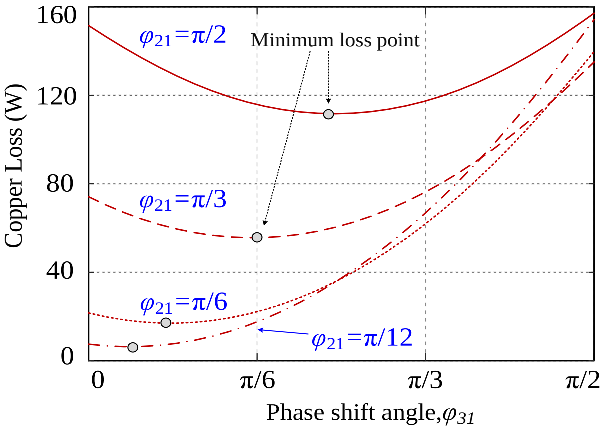

Fig.15. Copper loss of the magnetic link in TAB mode

$$R_{ins} = \frac{d_i}{k_i A_i} \tag{39}$$

where d_i , A_i and k_i are thickness, surface area and thermal conductivity of the insulation layer respectively. The thermal resistance of the inner and outer insulation layers are calculated from

$$R_{ins} = \frac{1}{2\pi k_i h_i} \ln\left(\frac{r_{out}}{r_{in}}\right) \tag{40}$$

where r_{in}, r_{out} and h_i are the inner diameter, outer diameter and height of the insulator respectively. The thermal resistance of the surrounding area depends on the characteristics of the media and can be nonlinear. To calculate the thermal resistance of the surrounding area, both convection and radiation effects should be considered. The convection thermal resistance (R_{con}), and the heat transfer coefficient (h_{con}) are defined from

$$R_{con} = \frac{1}{h_{con} A} \quad , \quad h_{con} = \frac{N_u k_m}{L} \tag{41}$$

where A is the surface area, k_m is the Thermal conductivity of the medium, N_u is the Nusselt number, and L is the characteristic length. The value of Nusselt number depends on some parameters which are discussed in [38]. The radiative thermal resistance (R_{rad}) and the radiative thermal coefficient (h_{rad}) are calculated from

$$R_{rad} = \frac{1}{h_{rad} A} \quad , \quad h_{rad} = \varepsilon \sigma (T_s + T_a)(T_s^2 + T_a^2) \tag{42}$$

where ε is the emissivity of the surface, T_s is the surface temperature, T_a is the ambient temperature and σ is the Steffan-Boltzmann’s constant and their values are presented in Table.III/Appendix.

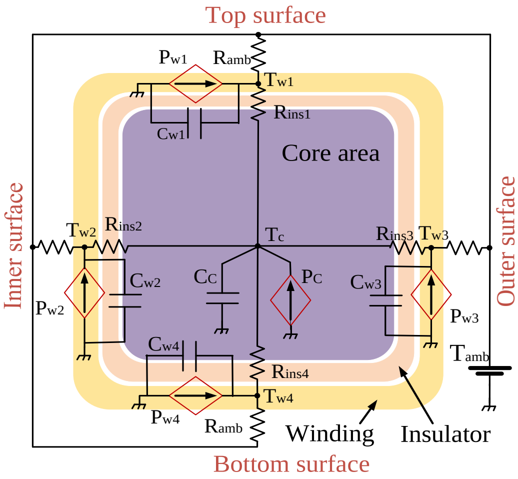

Fig. 16. Equivalent thermo-electric mode of the magnetic link.

As the radiation and convection thermal losses occur at the same time at the core or winding surface, the parallel connection of both resistances is presented as total thermal resistance of the surrounding area (R_{amb}) [38]. The heat sources in the model are calculated based on the core and copper losses resulted from previous stages of design. Therefore the effects of amplitude, phase shift and duty ratio of the supplied voltages and currents on the temperature rise have been taken into account. To define the value of heat sources resulted from copper loss in the winding, a constant value of dissipated heat per conductor length is assumed. The value of heat sources in each direction x, is equal to the total copper loss in the winding, (P_{cu}), calculated using (19), times the fraction of the length of a turn in the respective direction (l_x) to the length of a turn (L_n).

$$P_{cu,x} = P_{cu}\frac{l_x}{L_n} \tag{43}$$

On the other hand, the heat sources due to the core loss are determined according to their represented volume of the magnetic core from

$$P_{cx} = P_v \rho_c V_x \tag{44}$$

where P_v is specific core loss (in W/kg) calculated from (12), ρ_c is mass density of the core material (2605SA1) and V_x is the represented volume of the core covered by the winding. The temperature of the surrounding area is modeled as a constant voltage source, assuming negligible thermal effects of the magnetic structure on the ambient temperature. The thermal capacitances of the nodes are used to model the transients and are calculated based on the component's specific heat capacity [49]. They are connected in parallel to the current sources and are equal to zero for steady state analysis. Once all components of the equivalent thermo-electric model are defined, the energy balance equations are used to determine the temperature of selected hot points on the surface. The equation for central node of the circuit is written as

$$C_c\frac{dT_c}{dt} = \frac{1}{R_{ins1}}(T_{w1}-T_c)+\frac{1}{R_{ins2}}(T_{w2}-T_c)+\frac{1}{R_{ins3}}(T_{w3}-T_c)+\frac{1}{R_{ins4}}(T_{w4}-T_c)+P_c \tag{45}$$

where T_c, P_c, T_w and P_w are temperature and the magnetic loss in the core, winding temperature and copper loss respectively. On the other hand, the equation for the top layer node (T_W) considering R_{ins} as the thermal resistance of insulator, and R_{amb} as surrounding area, is defined by

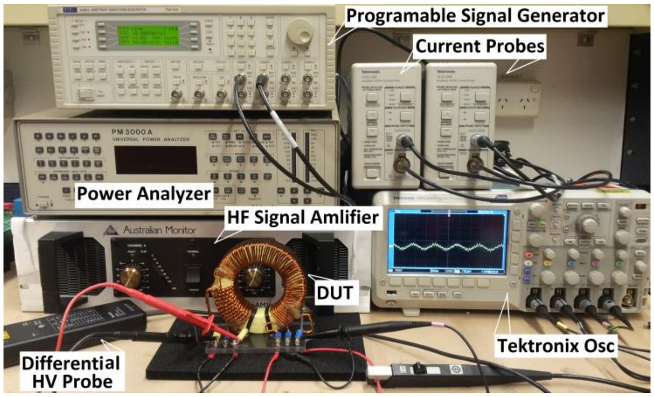

Fig. 17. Experimental test platform for core loss measurement

$$C_{w1}\frac{dT_{W1}}{dt} = \frac{1}{R_{ins}}(T_c - T_{w1}) + \frac{1}{R_{amb}}(T_{amb} - T_{w1}) + P_{w1} \tag{46}$$

The temperature on bottom, inner and outer layers can be found by writing same equations as (46). As windings are not distributed symmetrically around the core and have different conduction losses, the thermal model is considered separately for each of the three windings with the same central node temperature (T_C). Due to the dependency of the thermal model parameters on the temperature, an iterative solution based on the Newton-Raphson method was applied to the equations. To find the temperature rise at the core surface in steady state condition, the capacitances C_c and C_w are assumed equal to zero. To start the analysis, the initial temperature of all nodes is assumed to be equal to the ambient temperature and then parameters are evaluated in each iteration [39]. The resultant values of temperature at the center and surfaces of the magnetic core in steady state are compared with the specified thermal rise limit to redesign the magnetic structure in the case that they exceed the desired value (ΔT=45°C).

V. Experimental Tests and Validation

A prototype of a three-winding high-frequency toroidal magnetic link was developed for the proposed renewable energy system introduced in section II. The amorphous high-frequency toroidal core was made in our lab using thin tape of *Metglas 2605SA1*. The tape was glued with *Araldite 2011* epoxy adhesive on the surface of each layer and wound around a cylindrical frame. To reduce the skin and proximity effects, Litz wires with the strand diameter of 0.35 mm (27 AWG) are selected based on the lookup table recommendations. The number of isolated strands, S_n are calculated from (47) during the design procedure.

$$S_n = \frac{4i}{J\pi d^2} \tag{47}$$

where i is the winding's nominal current, J is the current density and d is the minimum diameter of a single strand of the Litz wire. The number of twisted insulated strands for windings one, two and three was defined as 18, 45 and 30 and their number of turns resulting from the design process was 45, 11 and 16 turns respectively. The overall diameters of twisted wires for the windings were measured approximately equal to d_1=1.9 mm, d_2=3.8 mm and d_3=2.75 mm.

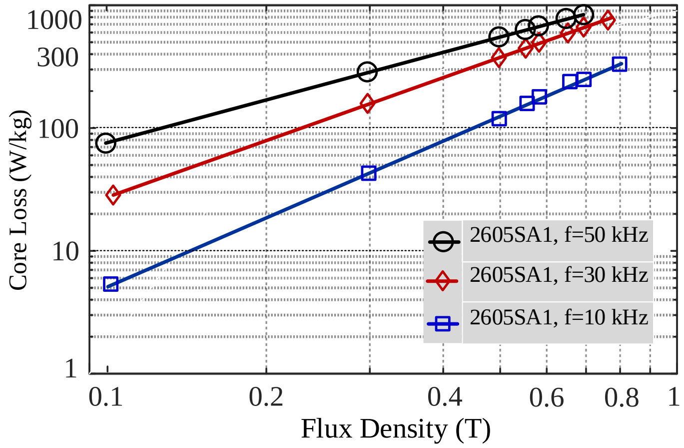

(b)

Fig. 18. Measured core loss of *Metglas 2605SA1* for 10, 30 and 50 kHz excitation currents.

A. Core loss measurement

An experimental test platform was established to measure the magnetic and electrical characteristics of the designed component as shown in Fig.17. The core loss of the magnetic link under square wave excitation current is measured experimentally. A TTi-TGA1244 programmable waveform generator was used as the main excitation source and the waveforms are amplified using high-frequency signal amplifier AM3002. The current and the voltage waveforms are observed using Tektronix current measurement probe TCPA300 and high-voltage differential probe P5200 respectively, and the total core and copper losses were measured using a power analyzer PM3000A.

The total loss (core loss plus copper loss) was measured using the power analyzer. To measure the copper loss, the ac resistances of windings related to each harmonic of the currents (main harmonics only) and the amplitude of the harmonics are measured using Instek LCR meter and spectrum analyzer respectively. The resultant copper loss is subtracted from total measured loss to find the core loss. Fig.18 presents the measured core loss for three cases of 10, 30 and 50 kHz (Fundamental, second and third harmonics of the switching frequency). To validate the core loss calculation method using IGSE, the specific core loss of the magnetic link was measured experimentally for frequency of 10 kHz and a wide range of zero voltage angle Ω, starts from 0 to $17\pi/18$. The variable duty ratio voltage is applied to port three as PV port and a constant duty ratio voltage (D=1) was applied to port one as reference port (V1=300 V, V3=90 V and $\varphi_{31}=\pi/3$). The experimental results are compared with the analytical calculations using three empirical loss calculation methods, OSE, IGSE and WcSE as presented in Fig.19 (a). As can be seen, increasing the zero-voltage angle, Ω (reducing the duty ratio) of the applied voltage, reduces the peak magnetic induction B_{max} and the magnetic loss density for all cases. Fig.19 (b) shows the values of specific core loss normalized to OSE to eliminate the downward behavior of the magnetic induction reduction and highlights the effects of the rate of change of magnetic induction. As expected the IGSE method presented less error compared to the other methods especially in higher zero-voltage angles however, the error increases for higher zero-voltage angles and small values of core loss. As in our application the duty ratio control is applied to the PV port, the zero-voltage angle is limited to $3\pi/4$ due to the limits of PV output power. In this range, the IGSE provided acceptable accuracy for loss calculation of the magnetic link.

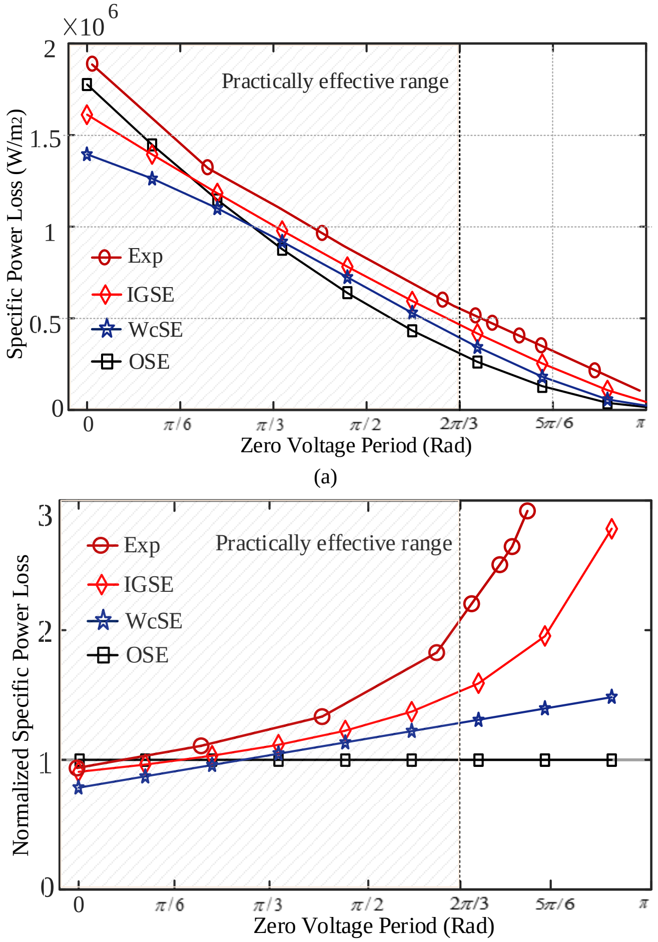

(a)

(b)

Fig. 19. Comparison of calculated and experimentally measured core loss using OSE, IGSE and WcSE calculation methods. Exciting voltages are applied to port three (Ω=0 to π, V3=90 V) and port one (D= 1, V1=300 V) and phase shift $\beta=\pi/3$, (a) Specific core loss, and (b) Normalized specific core loss to OSE method.

B. Copper loss measurement

The calculated and measured values of copper loss are compared for two cases of DAB and TAB operation modes, to find the accuracy of the harmonic based analysis. In the case of the DAB mode, a variable duty ratio voltage (Ω=0 to $\pi/2$) was applied to the PV port and a constant duty ratio voltage (D= 1) was applied to port one as reference port (f=10 kHz, V1=300 V, V3=45V-110 V). The test was carried out for same load and two different phase shift angles, $\varphi_{31}=\pi/8$ and $\varphi_{31}=\pi/2$. The zero-voltage angle Ω, has been changed from 0 to $\pi/2$ and the resultant copper loss is measured and is compared to the theoretically calculated values as presented in Fig.20 (a). As can be seen, increasing the zero-voltage angle rises the copper loss although, it is more considerable at higher phase shift angles. The experimentally measured values validate the analytical calculations although, the error increases at lower values of copper loss and higher zero voltage angles which can be attributed to the accuracy of the measurement instruments.

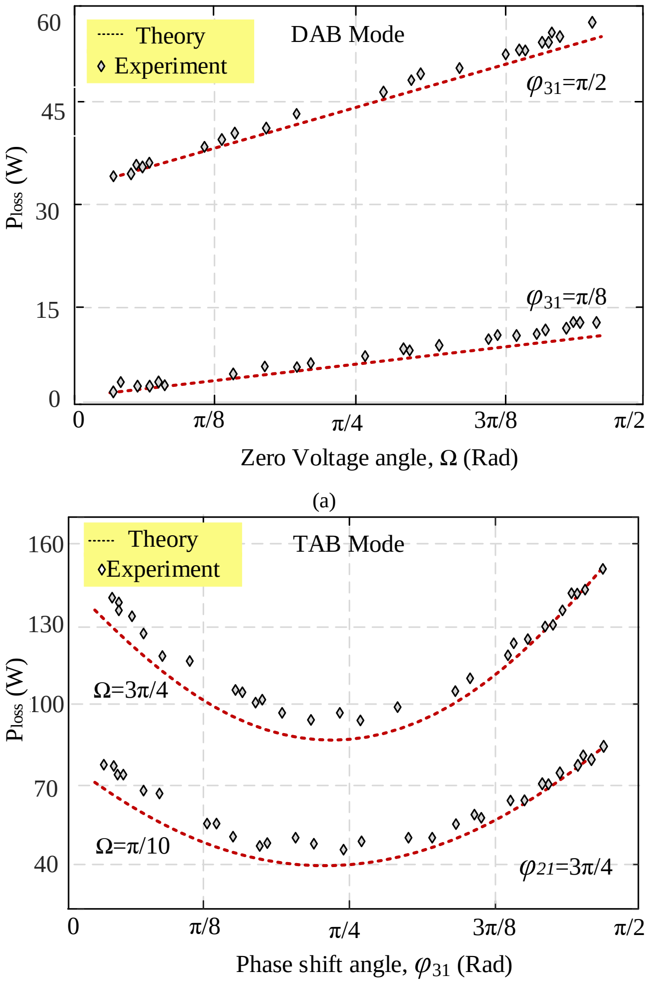

(a)

(b)

Fig. 20. Comparison of calculated and experimentally measured conduction loss for a). Zero voltage angle varies from Ω=0 to π/2 and two cases of phase shift angles, β=0 and β=π/2, b). Phase shift angle, β varies from 0 to π/2 and two cases of zero voltage angle, Ω= π/10 and Ω= 3π/4.

In the case of the TAB operation mode, the copper loss is measured for two cases of zero voltage angle, Ω= π/10 and Ω= 3π/4 where the phase shift angle in the PV port (φ_{31}), ranges from 0 to π/2 and φ_{21}=π/2. As is presented in Fig.20 (b), the copper loss of the magnetic link under the nominal load condition is minimized at φ_{31}=π/4 as discussed in section IV-D.

The difference between theoretically calculated and experimentally measured values was less than 10 % and decreased to less than 5% for higher phase shift angles. Based on the experimental test results, accuracy of the harmonic based copper loss analysis was confirmed.

C. Measurement of the temperature rise

To validate the accuracy of thermal analysis based on the proposed thermo-electric model, the temperature of the magnetic link was monitored and recorded for various load conditions and was compared to the theoretically calculated results. An infrared thermal camera, Flir-OSXL-I7 with the temperature resolution of 0.1ºC and adjustable emissivity of 0.1 to 1, was used to measure the thermal radiation of the winding and magnetic core. The surrounding of the core was covered with black cards to reduce the reflections. Fig.21 (a)-(c), shows the thermal images of the magnetic link under three different load conditions (Ambient temperature=27ºC, Emissivity=0.96). The temperature of the windings and the surface of the magnetic core were measured in steady state (1 ºC per 20 min change) for a range of power starts from 10 % to 100 % of nominal value. The maximum observed temperature was recorded for winding one as output port of the converter. As can be seen in Fig.21 (d), the winding temperature rise for maximum loss did not exceed 38 ºC (Overall temperature of 65 ºC) and the core temperature remained under 50 ºC. The resultant error was less than 8 % which confirmed the accuracy of the thermal analysis.

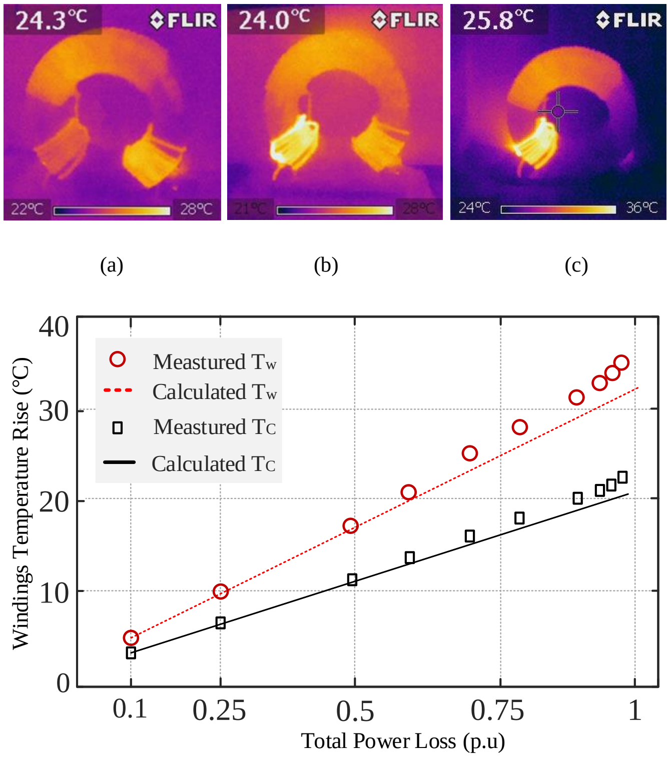

(a)

(b)

(c)

Fig.21. Thermal image of the magnetic link under three different load conditions, (a).Power transfers from W2 and W3 to W1, (b). Power transfers from W2 and W3 to W1, (c), Power from W3 to W1, and (d) temperature rise of the magnetic link.

D. Measurement of inductive and resistive elements

To evaluate the design procedure and measure the transformer parameters, an experimental test platform was established. The conventional short and open circuit tests have been widely used to measure the parameters of the magnetic components. The short-circuit test loses its accuracy when the winding resistances and the leakage reactances have relatively significant values compared to the magnetizing impedance and also a big difference between the primary and secondary leakage inductances and winding resistances. On the other hand, the value of the magnetic flux should be kept almost constant during all test procedures to achieve consistent results and it is difficult to maintain the same magnetizing current in the short circuit test compared to the open circuit test [39].

Table. II. Equations that are used to define the parameters of the magnetic link

Test Parameter	Differentially coupled and open circuit tests	Cumulatively coupled and open circuit tests	Combination of all three tests
R_{W1}	$\frac{(2N_{31}-1)R_1(OC)-R_3(OC)+R_{13}(dif)}{2N_{31}}$	$\frac{(2N_{31}+1)R_1(OC)+R_3(OC)+R_{13}(cum)}{2N_{31}}$	$R_1(OC)-\frac{R_{13}(cum)-R_{13}(dif)}{4N_{31}}$
R_{W3}	$\frac{(2-N_{31})R_3(OC)-N_{31}R_1(OC)+N_{31}R_{13}(dif)}{2}$	$\frac{(2+N_{31})R_3(OC)+N_{31}R_1(OC)-N_{31}R_{13}(cum)}{2}$	$R_3(OC)-\frac{N_{31}R_{13}(cum)-N_{31}R_{13}(dif)}{4}$
R_m	$\frac{R_3(OC)+R_3(OC)-R_{13}(dif)}{2N_{31}}$	$\frac{R_{13}(cum)-R_1(OC)-R_3(OC)}{2N_{31}}$	$\frac{R_{13}(cum)-R_{13}(dif)}{4N_{31}}$
L_{l1}	$\frac{(2N_{31}-1)L_1(OC)-L_3(OC)+L_{13}(dif)}{2N_{31}}$	$\frac{(2N_{31}+1)L_1(OC)+L_3(OC)-L_{13}(cum)}{2N_{31}}$	$L_1(OC)-\frac{L_{13}(cum)-L_{13}(dif)}{4N_{31}}$
L_{l3}	$\frac{(2-N_{31})L_3(OC)-N_{31}L_1(OC)+N_{31}L_{13}(dif)}{2}$	$\frac{(2+N_{31})L_3(OC)+N_{31}L_1(OC)-N_{31}L_{13}(cum)}{2}$	$L_3(OC)-\frac{N_{31}L_{13}(cum)-N_{31}L_{13}(dif)}{4}$
L_{13}	$\frac{L_1(OC)+L_3(OC)-L_{13}(dif)}{2N_{31}}$	$\frac{L_{13}(cum)-L_1(OC)-L_3(OC)}{2N_{31}}$	$\frac{L_{13}(cum)-L_{13}(dif)}{4N_{31}}$

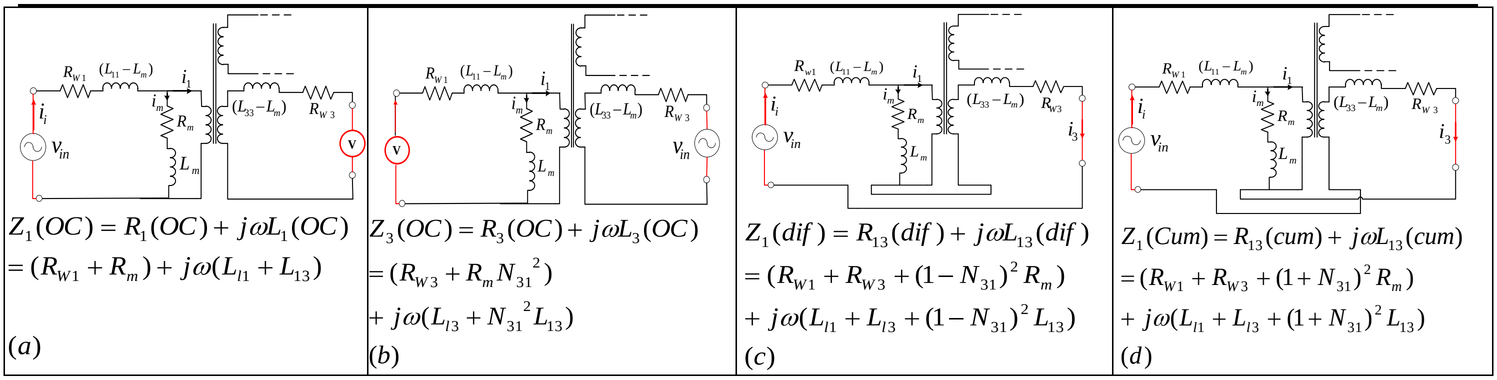

$$Z_1(OC)=R_1(OC)+j\omega L_1(OC)$$
$$=(R_{W1}+R_m)+j\omega(L_{l1}+L_{13})$$
(a)

$$Z_3(OC)=R_3(OC)+j\omega L_3(OC)$$
$$=(R_{W3}+R_m N_{31}{}^2)$$
$$+j\omega(L_{l3}+N_{31}{}^2L_{13})$$
(b)

$$Z_1(dif)=R_{13}(dif)+j\omega L_{13}(dif)$$
$$=(R_{W1}+R_{W3}+(1-N_{31})^2R_m)$$
$$+j\omega(L_{l1}+L_{l3}+(1-N_{31})^2L_{13})$$
(c)

$$Z_1(Cum)=R_{13}(cum)+j\omega L_{13}(cum)$$
$$=(R_{W1}+R_{W3}+(1+N_{31})^2R_m)$$
$$+j\omega(L_{l1}+L_{l3}+(1+N_{31})^2L_{13})$$
(d)

Fig.22. Experimental tests of magnetic link and related equations (a) secondary open circuit test, (b) primary open circuit test, (c) series coupling-differentially coupled test, and (d) series coupling-cumulatively coupled test

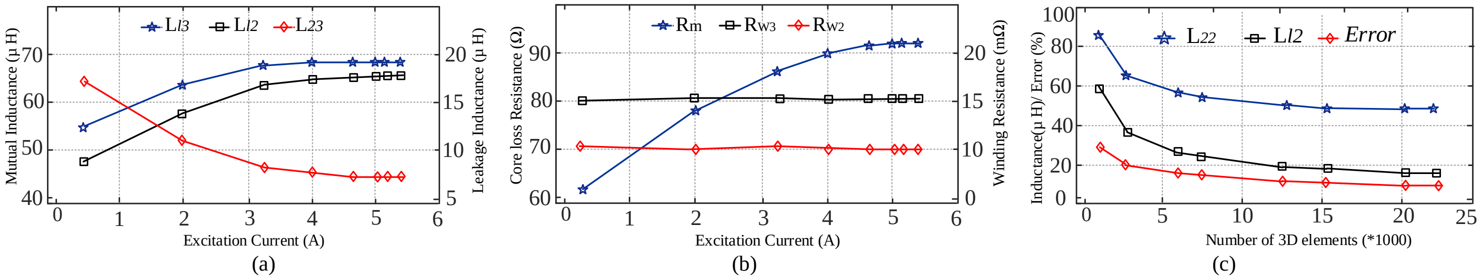

(a) (b) (c)

Fig.23 Experimental measured parameters of the winding one, (a) inductive elements, (b) resistive elements and, (c) inductive elements and resulting error.

Due to these problems, the short circuit test was excluded from our test procedure. To characterize the magnetic link, the conventional open circuit and the differentially and cumulatively coupled tests were applied to the windings [42]. The advantage of the series coupling tests over the short and open circuit test is that the series coupling tests can be used additionally to factor in the effects on the leakage and the magnetizing inductances of the windings. On the other hand, the measured resistances and inductances during the tests are the algebraic addition and subtraction of transformer parameters, which facilitate the direct measurements by the meter [39]. To study the experimental test procedure, only windings one and three are considered although the test process was applied similarly to the other pairs (windings one and two or windings two and three). The test circuit schematics and the measured impedance equations of each test are presented in Fig.22. In the presented equations *n* is the turns ratio of the windings three to one. The real and imaginary parts of the measured impedances are used to define the parameters of the magnetic link using equations in Table.II. The final value of each parameter is obtained from averaging the resultant values of the presented equations in the involved tests due to the presented excellent correlation. The value of the magnetizing flux density into the core should be kept constant during all the tests. Based on this, the following relationships between the excitation current during the tests should be considered [39], [42].

$$I_p=nI_s=I_{dif}(1-n)=I_{cum}(1+n) \tag{48}$$

where I_P, I_s, I_{dif} and I_{cum} denote the primary, secondary, differentially and cumulatively coupled test currents respectively. The values of resistances and inductances of windings two and three with the excitation current ranging from 0.5 to 5.5 A are measured. Fig.23 (a) shows that for any increase in the excitation current the mutual inductance between the windings two and three decreases while their leakage inductance increases slightly. On the other hand, Fig.23 (b) presents the measured values of resistive elements of the magnetic link. It was seen that the value of equivalent core loss resistance increases with increasing the test current while the winding resistances are independent of the test current and remain constant. The measured inductances are compared to the numerically calculated values to find the accuracy of the design process and field analysis using RNM as presented in Fig.23 (c). Comparing the calculated and the measured values shows the reduction of error to less than 10 % in the case of considering 22176 3D elements with a total computation time of 310 seconds. Further increase in the number of elements only increased the computation time without considerable effect on the error. The resultant error can be attributed to various experimental factors that cannot be included properly in the numerical analysis, such as stacking factor of the magnetic core, windings distribution and the core geometry.

VI. Conclusion

This paper studied all stages of design, prototyping and validity tests of a high-frequency toroidal magnetic link. The RNM was used to determine the dimension of the magnetic core and the windings for certain specifications due to the low computation time and acceptable accuracy. The core loss, copper loss and temperature rise of the component are evaluated as a part of the design procedure. The high-frequency skin and proximity effects and non-sinusoidal effects of the voltage and current waveform have been taken into account. The stored magnetic energy method is used to design the inductive elements of the magnetic link with less than 10 % error. The core loss is evaluated using the IGSE method for non-sinusoidal voltages and their main harmonics (10, 30 and 50 kHz). It was seen that the core loss increases with increasing zero-voltage angle of the applied voltages. The copper loss is calculated based on the harmonic content of the non-sinusoidal excitation currents and the ac resistance of the windings considering skin and proximity using modified Dowell's equation. It was seen that in the case of DAB operation mode, the copper loss raised with increasing zero-voltage angle and phase shift angle. In the case of TAB operation mode, there is a minimum copper loss point where the phase shift in one port is half of the second one. The harmonic based analysis estimated the copper loss with a reasonable accuracy (error between 5 to 10 %). A thermo-electric model is used to evaluate the temperature rise using estimated loss components. The series-coupling, cumulatively and differentially tests along with conventional open-circuit test have been successfully used to measure the inductive and resistive parameters of the magnetic link.

Appendix

A. Parameters of the design and experimental tests

Table. III. Theoretical and experimental parameters

Description	Value
Electrical Parameters	
Nominal power (kVA)	P=4.5
Nominal power of each winding(kVA)	P_{W1}=2, P_{W2}=1.5, P_{W3}=1
Nominal windings voltage	V_{W1}=300V,V_{W2}=60V,V_{W3}= 30-110V
Number of turns	N1 : N2 : N3= 52 : 12 :8
Operating frequency	10 kHz
Required leakage inductance	L_{l2}=14μH,L_{l1}=35μH,L_{l3}=18μH,
Magnetizing inductance	L_m= 50 μH
Magnetic Parameters	
Core material	Amorphous, 2605SA1
Magnetic core shape	Toroidal
Magnetic core dimension	r_{in}(mm)=32.5,r_{out}(mm)=52.5 h(mm)=25 , w(mm)=20
Maximum flux density	B_m=1.2 T
Magnetic permeability	26000
Mass density, 2605SA1	7.18 G/cm^3
Curie temperature, 2605SA1	395 ºC
Loss Analysis Parameters	
Maximum operating temperature	T_{max}=65 ºC
Dimensions of the magnetic tape	25mm width /20 μm thickness
Litz wire strand diameter	27 AWG / 0.35 mm
Insulation tape material	Polyvinyl chloride (PVC)
Insulation thickness	Thickness=0.2 mm
Stacking factor	0.94
Resistivity factor of copper conductor	1.7*10.E-8 Ω.m
Conductivity of copper conductor	58.5*10.E+6 Siemens/m
DC resistance of windings (mΩ)	$R_{dc\text{-}w1}$=45, $R_{dc\text{-}w2}$=9, $R_{dc\text{-}w3}$=17
Permeability of copper conductor	1.256*10.E-6 H.m^{-1}
Maximum current density	4 A.mm^{-2}
Thermal Analysis Parameters	
Emissivity of insulator tape	0.87
Emissivity of coated conductors	0.97
Stefan Bultzman constant	5.670367*10.E−8 W.m^{-2}.k^{-4}
Thermal conductivity of copper	401 W/m.k
Thermal conductivity of insulator	0.19 W/m.k
Thermal conductivity of air	0.024 W/m.k
Heat transfer coefficient of the air	24 W/m^2.k

References

[1] M. R. Islam, Y. G. Guo, Z. W. Lin, and J. G. Zhu, "An amorphous alloy core medium frequency magnetic-link for medium voltage PV inverters," *J. Appl. Phys.*, vol.115,no.17,pp. 17E710 - 17E710-3, May 2014.

[2] Y. M. Chen, Y. C. Liu, and T. F. Wu, "Multi-input dc–dc converter based on the multi-winding transformer for renewable energy applications," *IEEE Trans. Ind Applications*, vol. 38, no. 4, pp. 1096–1104, July/August 2002

[3] T.Ma, H. Yang, and L.Lu, "Development of hybrid battery–supercapacitor energy storage for remote area renewable energy systems," *Applied Energy*, Vol.153, pp. 56-62, 2015

[4] J.Li, R.Xiong, Q.Yang, F.Liang, M.Zhang, and W.Yuan, "Design/test of a hybrid energy storage system for primary frequency control using a dynamic droop method in an isolated microgrid power system,",*Applied Energy*,Vol.201,pp.257-269,2017

[5] H. Tao, J. L. Duarte, M. A. M. Hendrix, "Three-port triple-half bridge bidirectional converter with zero voltage switching," *IEEE Trans. Power Electron*, vol. 23, no.2, pp 782–792, March 2008.

[6] M. McDonough, "Integration of Inductively Coupled Power Transfer and Hybrid Energy Storage System: A Multiport Power Electronics Interface for Battery-Powered Electric Vehicles," *IEEE Tran. Power Electron*, vol. 30, no. 11, pp. 6423-6433, Nov. 2015

[7] Y. Chen, X. Liu, Y. Cui, J. Zou and S. Yang, "A Multi Winding Transformer Cell-to-Cell Active Equalization Method for Lithium-Ion Batteries With Reduced Number of Driving Circuits," *IEEE Tran. Power Electron*, vol. 31, no. 7, pp. 4916-4929, July 2016.

[8] H. Tao, A. Kotsopoulos, J. L. Duarte, and M. A. M. Hendrix, "Family of multiport bidirectional DC-DC converters," *IEE Proceeding Electric Power Applications*, vol. 153, no. 3, pp. 451–458, May 2006.

[9] A. Davoudi, P. L. Chapman, J. Jatskevich and H. Behjati, “Reduced-Order Dynamic Modeling of Multiple-Winding Power Electronic Magnetic Components,” *IEEE Trans. Power Electron*, vol. 27, no. 5, pp. 2220-2226, May 2012.

[10] Chunyang Gu, Zedong Zheng, Lie Xu, Kui Wang and Yongdong Li, “Modeling and Control of a Multiport Power Electronic Transformer (PET) for Electric Traction Applications,” *IEEE Trans. Power Electron*, vol. 31, no. 2, pp. 915-927, Feb. 2016.

[11] J.Wang et al., “Derivation, calculation, and measurement of parameters for a multi-winding transformer electrical model,” *IEEE APEC 1999*, pp. 220-226.

[12] E. S. Hamdi, Design of Small Electrical Machines. Chichester, U.K.: Wiley, 1998.

[13] T. A. Lipo, Introduction to AC Machine Design. Madison, WI: Wisconsin Power Electronics Research Center, Univ. of Wisconsin-Madison, 2004.

[14] T. W. Preston and J. P. Sturgess, “Implementation of the finite-element method into machine design procedures,” in *Proc. Int. Conf. Electr.Mach.Drives*, 1993, pp. 312–317.

[15] S. R. H. Hoole, A. Mascrenghe, K. Navukkarasu, and K. A. S. K. Sivasubramaniam, “An expert design environment for electrical devices and its engineering assistant,” *IEEE Trans. Magnetics.*, vol. 39, no. 3, pp. 1693–1696, May 2003.

[16] J. Perho, “Reluctance network for analysing induction machines,” *Acta Polytech. Scand., Electr. Eng. Series*, vol. 110, pp. 1–147, Dec. 2002.

[17] A. Souissi, M. W. Zouaghi, I. Abdennadher and A. Masmoudi, “MEC-Based Modeling and Sizing of a Tubular Linear PM Synchronous Machine,” *IEEE Trans. Ind Applications*, vol. 51, no. 3, pp. 2181-2194, May-June 2015

[18] E. R. Laithwaite, “Magnetic equivalent circuits for electrical machines,” Proc. Inst. Electr. Eng., vol. 114, no. 11, pp. 1805–1809, Nov. 1967.

[19] C. J. Carpenter, “Magnetic equivalent circuits,” Proc. *Inst. Electr. Eng*., vol. 115, no. 10, pp. 1503–1511, Oct. 1968.

[20] V. Ostovi´c, “Magnetic equivalent circuit presentation of electric machines,” *Electr. Mach. Power Syst*., vol. 12, no. 6, pp. 407–432, Jun. 1987.

[21] B. Auchmann, B. Flemisch, and S. Kurz, “A discrete 2-D formulation for 3-D field problems with continuous symmetry,” *IEEE Trans. Magnetics,* vol.46 , no.8 , pp.3508–3511, Aug. 2010.

[22] R. Wang, S. Pekarek, M. L. Bash, A. Larson and R. V. Maaren, “Incorporating Dynamics in a Mesh-Based Magnetic Equivalent Circuit Model of Synchronous Machines,” *IEEE Trans. Energy Conversion*, vol. 30, no. 3, pp. 821-832, Sept. 2015.

[23] H. Gorginpour, H. Oraee and R. A. McMahon, “A Novel Modeling Approach for Design Studies of Brushless Doubly Fed Induction Generator Based on Magnetic Equivalent Circuit,” *IEEE Trans. Energy Conversion*, vol. 28, no. 4, pp. 902-912, Dec. 2013.

[24] M. Amrhein and P. T. Krein, “3-D Magnetic Equivalent Circuit Framework for Modeling Electromechanical Devices,” *IEEE Trans. Energy Conversion*, vol. 24, no. 2, pp. 397-405, June 2009.

[25] C. P. Steinmetz, “On the law of hysteresis,” *AIEE Trans.*, vol. 9, pp. 3-64, Sep. 1892.

[26] I. Villar, U. Viscarret, I. Etxeberria-Otadui and A. Rufer, “Global Loss Evaluation Methods for Nonsinusoidally Fed Medium-Frequency Power Transformers,” *IEEE Trans. Industrial Electronics*, vol. 56, no. 10, pp. 4132-4140, Oct. 2009.

[27] J. Reinert, A. Brockmeyer, and R. W. A. A. De Doncker, “Accurate calculation of losses in ferro- and ferrimagnetic materials based on the modified Steinmetz equation,” *IEEE Trans. Ind. Appl.*, vol. 37, no. 4, pp. 1055–1060, Jul./Aug. 2001

[28] A. Van den Bossche, V. C. Valchev, and G. B. Georgiev, “Measurement and loss model of ferrites with non-sinusoidal waveforms,” in *Proc. 35th Annu. IEEE PESC*, Jun. 20–25, 2004, vol. 6, pp. 4814–4818.

[29] K. Venkatachalam, C. R. Sullivan, T. Abdallah, and H. Tacca, “Accurate prediction of ferrite cores loss with nonsinusoidal waveforms using only Steinmetz parameters,” in *Proc. IEEE Workshop Comput. Power Electron.*, Jun. 3–4, 2002, pp. 36–41.

[30] W. Shen, “Design of high-density transformers for high-frequency highpower converters,” Ph.D. dissertation, Virginia Polytechnic Inst. State Univ., Blacksburg, VA, Jul. 2006.

[31] C. R. Sullivan, “Computationally efficient winding loss calculation with multiple windings, arbitrary waveforms, and two-dimensional or three-dimensional field geometry,” *IEEE Trans. Power Electron.*, vol. 16, no. 1, pp. 142-150, Jan 2001

[32] R. P. Wojda and M. K. Kaizimierczuk, “Winding resistance of litz-wire and multi-strand inductors,” *IET Power Electron*., vol. 5, no. 2, pp. 257–268, Feb. 2012

[33] P.L. Dowell, “Effects of eddy currents in transformer windings,” *in Proc. IEE,* Vol.113, pp.1387-1394, Aug. 1966

[34] J. A. Ferreira, “Improved analytical modeling of conductive losses in magnetic components,” *IEEE Trans. Power Electron*, vol. 9, no. 1, pp. 127-131, Jan 1994.

[35] F. Tourkhani and P. Viarouge, “Accurate analytical model of winding losses in round litz wire windings,” *IEEE Trans. Magn*., vol. 37, no. 1, pp. 538–543, Jan. 2001

[36] X. Nan and C. R. Sullivan, “An equivalent complex permeability model for litz-wire windings,” *IEEE Trans. Ind. Appl*., vol. 45, no. 2, pp. 854–860, Mar./Apr. 2009

[37] R. Wrobel, A. Mlot and P. H. Mellor, “Contribution of End-Winding Proximity Losses to Temperature Variation in Electromagnetic Devices,” *IEEE Trans. Ind. Electron*, vol. 59, no. 2, pp. 848-857, Feb. 2012.

[38] S. Purushothaman and F. de Leon, “Heat-Transfer Model for Toroidal Transformers,” *IEEE Trans. Power Delivery*, vol. 27, no. 2, pp. 813-820, April 2012.

[39] J.G .Hayes, D. Cashman, M.G. Egan, T .O'Donnell, “Comparison of test methods for characterization of high-leakage two-winding transformers,” *IEEE Trans. Ind. Appl.* Vol.45,no.5, pp.1729 – 1741

[40] R. Burdt, R. C. Curry,K. F.McDonald, P.Melcher, R.Ness, and C.Huang,“ Evaluation of nanocrystalline materials, amorphous metal alloy, and ferrites for magnetic pulse compression applications,” *J. Appl. Phys.*, vol. 99,no. 8, pp. 08D911-1–08D911–3, Apr. 2006.

[41] Wm. Colonel and T. McLyman, *Transformer and Inductor Design Handbook*, 3rd ed. New York: Marcel Dekker, 2004.

[42] M. Jafari, Z. Malekjamshidi, G. Lei, T. Wang, G. Platt and J. Zhu, “Design and Implementation of an Amorphous High-Frequency Transformer Coupling Multiple Converters in a Smart Microgrid,” *IEEE Trans. Ind. Electron.*, vol. 64, no. 2, pp. 1028-1037, Feb. 2017.